Corrosion behavior of tantalum coatings on AISI 316L stainless steel substrate for bipolar plates of PEM fuel cells

Ángel Pérez Manso[1,§], Florencio Fernández Marzo[2], Xabier Garicano[1], Cinthia Alegre[3], Antonio Lozano[3], Félix Barreras[3]

[1] *Department of Graphic Expression and Engineering Projects, Faculty of Engineering, University of the Basque Country (UPV/EHU), Plaza Europa 1, 20018 San Sebastian, Spain*

[2] *Department of Chemical Engineering and Environment, Faculty of Engineering, University of the Basque Country (UPV/EHU), Plaza Europa 1, 20018 San Sebastian, Spain*

[3] *LIFTEC, CSIC-Univ. of Zaragoza, C/ María de Luna, 10. 50018, Zaragoza (SPAIN)*

Abstract

Corrosion resistance of tantalum coatings 30 µm thick deposited by chemical vapor deposition on SS316L coupons has been evaluated by electrochemical impedance spectroscopy (EIS). To this end, anodic and cathodic operating conditions of proton exchange membrane fuel cells (PEMFC) have been simulated in a three-electrode heated corrosion cell. Interfacial contact resistance (ICR), contact angle and durability tests have been performed in long-term tests (> 100 h) polarizing the electrode to 1.193 V *vs.* Ag/AgCl. Results obtained by different experimental techniques show a dense coating structure with a high polarization resistance, mainly formed by surface crystals of α-Ta (bcc), Ta_2O_5 and carbon. An atomic ratio (in %) of oxide to metallic species (Ta_{ox}/Ta_{met}) of 4.8 was verified from XPS spectra, which is slightly increased to 6.23 after the anodizing treatment. The modified surface composition yielded a coating capacity higher than the amorphous oxide, favoring the in-plane electrical conduction. After the treatment, no noticeable changes were observed neither in surface morphology nor in contact angle (>90°). ICR values in the range of 22.3 – 32.6 mΩ cm^2 were obtained for a clamping pressure of 140 N cm^{-2}. No morphological changes or loss of coating adherence were observed during the long-term tests.

Keywords: PEMFC; Stainless steel bipolar plates; tantalum coating; corrosion; EIS

§ Corresponding author: angel.perez@ehu.eus; Ph.: (+34) 943 018 673

NOMENCLATURE

Acronyms

bcc	Body-centered cubic structure
BP	Bipolar plate
CPE	Constant phase element
CVD	Chemical vapor deposition
DC	Direct current
EDX	Energy Dispersive X-rays
EIS	Electrochemical impedance spectroscopy
GDL	Gas diffusion layer
ICR	Interfacial contact resistance
PEMFC	Polymer electrolyte membrane fuel cell
SEM	Scanning electron microscopy
SHE	Standard hydrogen electrode
SS	Stainless steel
Ta	Tantalum
XPS	X-ray photoelectron spectroscopy
XRD	X-ray powder diffraction

Latin letters

C	Capacity (μF)
R	Resistance (Ω)
T	Fitting parameter
Z	Impedance (Ω)

Greek letters

ε	Dielectric constant
ε_o	Vacuum permittivity (8.885×10^{-12} F m^{-1})
δ	Thickness of the oxide layer (μm)

1.- INTRODUCTION

Researchers and engineers working on polymer electrolyte membrane fuel cells (PEMFCs) all over the world are striving to manufacture robust and reliable devices capable of ensuring a large lifetime under a wide range of operating conditions. However, despite the good results obtained in the last two decades, one of the main drawbacks that prevent PEMFCs to become practical energy systems is still the high cost/lifetime ratio. One of the relevant elements in the final cost of a stack is the bipolar plates (BPs) that can reach around 25% of the total, if a production of 500,000 units per year is considered [1,2]. Only the contribution of the catalyst has a larger impact on the total cost of an actual device.

BPs are key elements in PEMFC stacks. They are responsible for the homogenous distribution of the reactant gases to the different cells and over the electrodes, facilitate the extraction of water and excess of heat, and transport the electrons released cell by cell. To fulfill all these missions, used materials must combine high thermal and electrical conductivity, together with a good resistance to corrosion and surface hydrophobicity [3]. In general, materials employed in BPs are divided into metals and carbon-based composites [4], [5], [6], [7], [8], [9], [10], [11]. Initially, composites with high density graphite were mostly selected, due to their excellent chemical and electrical properties. However, its use has been limited to stacks for both stationary applications and research purposes, where weight and manufacturing costs are not critical factors. On the contrary, for mobile and transport applications, volume and weight are key parameters, and mass production processes are essential for reducing system costs [12]. Therefore, metal BPs have attracted the attention of the scientific community in recent years. The main disadvantage of metal plates for PEMFCs is the chemical instability, since the corrosion phenomena that take place in both anode and cathode sides due to the dissolution of metal cations can contaminate the polymeric membrane, reducing its proton conductivity [13]. In addition, formation of passive films on the metal surface increases the interfacial contact resistance (ICR) between BPs and gas diffusion layers (GDLs). Both processes eventually cause a significant drop in the efficiency and a drastic reduction in the useful lifetime of the electrochemical device.

To minimize the effects of metallic corrosion without reducing the electrical conductivity, different surface modification techniques have been proposed together with corrosion-resistant coatings [14], [15], [16], [17]. Different coatings have been tested, some of them based on noble metals [18], [19], metal carbides and nitrides [20], [21], [22], [23], as well as

Ni-based treatments [24], [25], among others. The goal is to protect the metal surface from the aggressive operating environment with a defect-free coating and a minimum ICR, to ensure both the correct performance and large lifetime of the stack. To use very thin sheets of stainless steel (SS) as BPs in PEMFCs, tantalum (Ta) coatings present an excellent corrosion resistance. Recently, different Ta-based compounds have been used as protective coatings for AISI 316L SS, applied with different techniques. Yu et al. [26] analyzed metallic Ta coatings deposited by physical vapor deposition (PVD), including corrosion tests of 1.1 hours combined with SEM, XRD and EDX. Other authors have focused on mono- and multi-layer coatings based on tantalum nitride deposited by sputtering techniques [27], [28], [29], [30], where long-term corrosion tests (up to 14 h) were combined with ICR and surface analysis techniques using SEM and XRD. Similarly, the behavior of Ta coatings on AISI 316L deposited by chemical vapor deposition (CVD) at high temperature (120°C) has been studied employing SEM and EDX [31]. On the other hand, Jensen et al. [32] analyzed the ICR between two surfaces of tantalum to be used in electrolyzers and high temperature PEMFCs (HT-PEMFCs).

Following the suggestions of the DOE [33], ex situ PEMFCs potentiodynamic and potentiostatic corrosion analyses must be performed in long-term tests (> 24h). However, little information on the durability of Ta coatings under these testing conditions can be found in the Literature. For this reason, the performance against corrosion of Ta-based coatings on AISI 316L substrates, deposited by CVD have been studied in the present research. Both PEMFCs anodic and cathodic operating conditions have been simulated in a three-electrode reactor. The behavior of the coatings under polarization potential of 1.193 V *vs.* Ag/AgCl in very long-term tests (> 100 h) has been also analyzed. To study the density of defects, their nature (amorphous or crystalline) and the characteristics of the anodic oxide formed by the Ta coating, ICR and contact angle tests were combined with SEM-EDX, XRD and XPS analysis. The effect of anodic polarization on the surface of the coating has been monitored by electrochemical impedance spectroscopy (EIS) using an equivalent electric circuit (EEC). Relevant information about the electrochemical corrosion process and the evolution of the dielectric properties of the coating with polarization time has been obtained.

2.- Material and methods

2.1.- Coating procedure

Probes consisted in manufactured disks of AISI 316L stainless steel with a diameter of 15 mm

and a thickness of 4 mm. Samples were previously polished with metallurgical paper of different grades, and further mirror-polished using an alumina solution with a grain of 0.1 µm. Prior to corrosion tests the probes were carefully cleaned with acetone, washed with distilled water and dried in a muffle at 50°C. A 30 µm thick Ta-based coating was then applied to the polished and cleaned samples by TANTALINE Denmark, using chemical vapor deposition (CVD).

2.2.- Corrosion measurements

Corrosion tests were carried out in a heated corrosion cell with a configuration of three-electrodes for DC tests (potentiodynamic and potentiostatic polarization), and four-electrodes for AC tests (EIS). In the three-electrode configuration, an Ag/AgCl reference electrode (3 M KCl, 207 mV *vs.* SHE), a working electrode (AISI 316L coated with Ta), and a counter electrode (Pt mesh) were used. Unless otherwise indicated, all the potentials appearing in this paper will be referred to the Ag/AgCl reference electrode. For the four-electrode configuration, the previous three electrodes were used together with a fourth Pt wire electrode connected to the reference electrode in parallel with a 10 nF capacitor [34]. The fourth electrode eliminates the electrical artifacts that appear in the impedance signal at high working frequencies. To eliminate signal interferences due to the low corrosion current density measured in the DC tests, a 5 Hz filter was also included in the setup of the software (PowerSuite-AMETEK Scientific Instruments), as well as a 5 Ω resistance connected in series with the working electrode [35]. To eliminate artifacts in the electrical signals during the impedance tests, another important issue is the relative position of the electrodes [36]. Based on previous studies, working and reference electrodes were both placed at 3 mm at both sides of the Pt wire, while the counter electrode was separated 5 mm from the working one.

Corrosion tests were performed with a Princeton Applied Research PARSTAT 2273 potentiostat-galvanostat controlled by the PowerSuite software, which was used to design both DC experiments (potentiodynamic polarization curves) and AC tests (EIS). EIS tests were performed after potentiostatic polarization experiments. The frequency range was scanned from 10 mHz to 100 kHz with an excitation amplitude of 10 mV. Analysis of the impedance spectra was performed by fitting the experimental results to equivalent electric circuits using the Zview 3.5 f software (Scribner).

The probes of Ta-coated AISI 316L SS for BPs (T1, T2 and T3 samples) were exposed to both anodic and cathodic simulated conditions, according to the recommendations of the DOE [37].

Anodic simulation tests (T1 sample) were carried out in an acid solution (H_2SO_4 + 0.1 ppm HF; pH 3; 80ºC). The working electrode was subjected to a potentiodynamic polarization of 0.1 mV/s between −0.4 V and +0.6 V, bubbling the corrosion cell with N_2. Long-term potentiostatic polarization experiments to +0.1 V were also carried out in this same electrolyte, with polarization steps of 5 min and a polarization cumulative total time of 27 h. After every polarization step an EIS test was performed at output cell potential, after stabilizing the potential of the working electrode. On the other hand, cathodic simulation tests (T2 sample) were carried out by potentiostatic polarization experiments at +0.6 V, using the same electrolyte as in the anodic simulation tests, but bubbling air into the corrosion cell to obtain an O_2 saturated solution. Again, EIS tests were performed after each polarization step. In addition, very long-term cathodic tests (> 100 h) were performed by combining potentiostatic polarization steps and EIS experiments (T3 sample) to a voltage of +1.193 V to simulate extreme operating conditions of PEMFC during startup/shutdown process and hydrogen starvation situations [38], [39]. The EIS experimental data were validated using the Kramers-Kronig relationships before analyzing the impedance data using an equivalent circuit model [40], [41], [42]. The reliability of the validity tests was confirmed by the analysis of the relative deviation between the ideal Kramers-Kronig fitted spectrum and the experimental data (Kramers-Kronig residuals test, %) [40]. After that, a physical model was proposed to fit the impedance spectra results to those obtained with a representative equivalent circuit model (ECM) elaborated using the Zview 3.5 f software (Scribner).

2.3.- Interfacial contact resistance (ICR)

ICR measurements were carried out following the procedure described in the literature, adopting an experimental configuration similar to Papadias et al. [43]. Temperature, tightening pressure, and current intensity circulating through the sample were carefully controlled during the tests. To perform the experiments, a device formed by a PTFE body was manufactured to hold the BP sample placed between two copper plates at a constant temperature of 80°C. The tightening pressure was applied using a TECNIMETAL MANUAL TEST STAND AST-J test bench in a range from 0 to 2 MPa, at 0.25 MPa steps. A Hewlett Packard 34401A voltmeter (0.1 μV resolution) was used to obtain the resistive values at a current of 1 A applied by a BLAUSONIC FA-210 power supply (0.001 A resolution). Connecting cables between the voltmeter and the copper plates were safety shielded to avoid any interference

in the signals. GDL discs of B1ASWP from E-TEK Inc. composed of a micro-porous tefloned layer over carbon paper with a total thickness of 400 μm, were used.

The procedure was developed in two steps. In the first one, the test was carried out considering only the GDL, in order to estimate the ICR between the GDL and the copper plates ($R_{CU/GDL}$), identified as R_{T2}. Secondly, a sandwich formed by a Ta-coated probe and GDL layers on each side was considered, obtaining the value of R_{T1}. Finally, the interfacial contact resistance, $R_{GDL/BP}$, was calculated as:

$$R_{GDL/BP} = \frac{(R_{T1} - R_{T2})}{2} \quad (1)$$

2.4.- Surface roughness and contact angle

The measurement of surface roughness was obtained using a Surface Roughness Tester from Mitutoyo, together with the SURFPAK® SJ v.3.002 surface texture analysis software. In addition, the contact angle was measured using a Phoenix 300 Touch equipment from Surface Electro Optics. All tests were performed at room temperature, using 5 μL drops of deionized water.

2.5.- SEM-EDX, XRD and XPS characterization

Both morphological and semi-quantitative chemical analyses of the Ta-coatings were performed by scanning electron microscopy with energy dispersive X-rays (SEM-EDX), using a JEOL JSM-6400 system. In addition, X-ray diffraction patterns (XRD) were collected with a Philips X'pert PRO automatic diffractometer operating at 40 kV and 40 mA, in theta-theta configuration, secondary monochromator with Cu-Kα radiation (λ = 1.5418 Å) and a PIXcel solid state detector (active length in 2θ = 3.347°).

X-ray photoelectron spectroscopy (XPS) measurements were performed in a SPECS system (Berlin, Germany) equipped with a Phoibos 150 1D-DLD analyzer and a monochromatic Al Kα radiation source (1486.7 eV), using the line C 1s (284.6 eV) for reference. An initial analysis was carried out to determine the existing elements (wide scan: step energy 1 eV, dwell time 0.1 s, pass energy 80 eV), and then the detailed analyses of the detected elements was performed (detail scan: step energy 0.1 eV, dwell time 0.1 s, pass energy 30 eV) with an electron exit angle of 90°. The spectra were fitted with the Casa XPS 2.3.16 software, which models the Gauss–Lorentzian contributions, after background subtraction (Shirley). Concentration values of each species were calculated using the atomic sensitivity factors from Scofield cross-sections and considering the instrumental transmission function and

corrections due to differences in the inelastic mean free path. From these values the atomic ratio (in %) of the oxide and metallic species of Ta (Ta_{ox} and Ta_{met} respectively) were calculated.

3.- Results and discussion

3.1. Surface morphology and structure

Figure 1 shows the SEM images of the Ta-coatings before being exposed to anodic polarization treatments. In Fig. 1a), a compact coating with an average thickness of 30 μm is observed, on which a columnar growth morphology with surface macropores is generated, as clearly depicted in Figs. 1c) and 1d). Micropores randomly distributed generated during the coating process are also observed in the compact zone of the coating (see red circles). Furthermore, the EDX linear scanning over the cross section of the coating shown in Fig. 1b) confirms the good adherence of the coating with the AISI 316L stainless steel base metal.

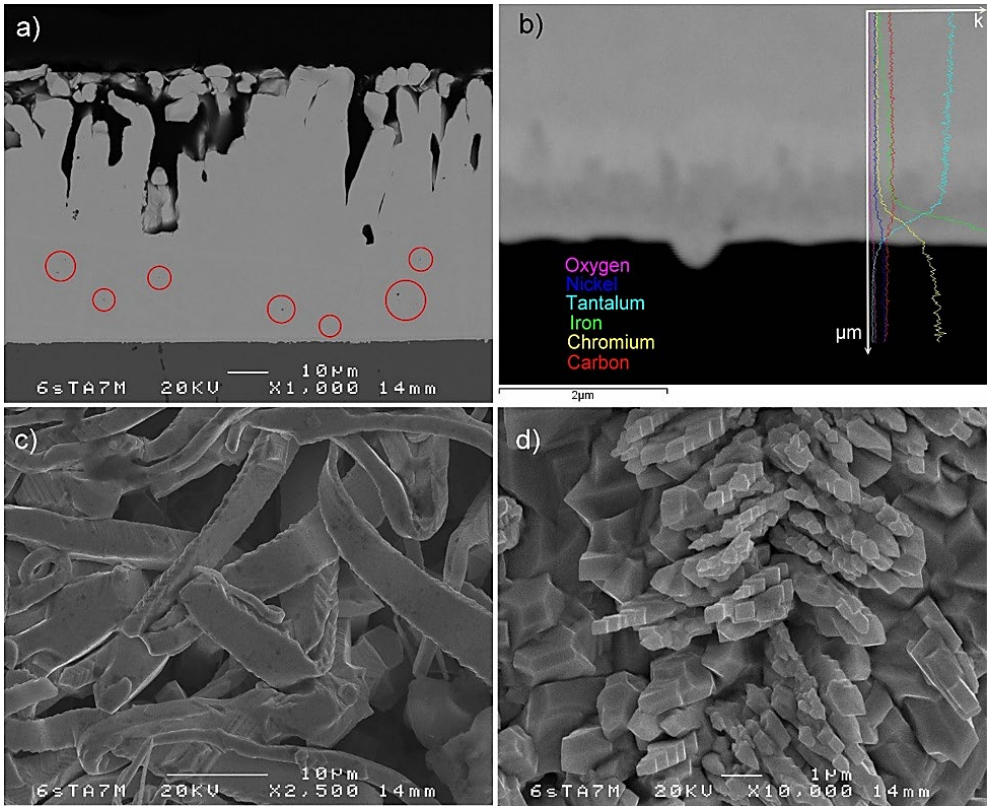

Figure 1. SEM image of the Ta coating as-deposited: a) cross-section; b) EDX linear scanning of cross section with the elements composition profiles; c) and d) coating surface with columnar growth morphology.

The tantalum can be presented in two different crystallographic phases: an α-phase with stable body-centered cubic structure (bcc), and a β-phase with tetragonal metastable

structure, which can evolve to the α-phase by thermal treatment at a high temperature (750 – 900°C) [44], [45]. Both α- and β-phases have very different electrical and mechanical properties [46], the α-phase being the one with the lowest resistivity (around 30 μΩ cm instead of more than 200 μΩ cm for the β-one). In this study, the XRD results presented in Fig. 2 confirm that the Ta coating is composed of α-Ta crystals, which is the suitable structure for BPs from an electrical point of view.

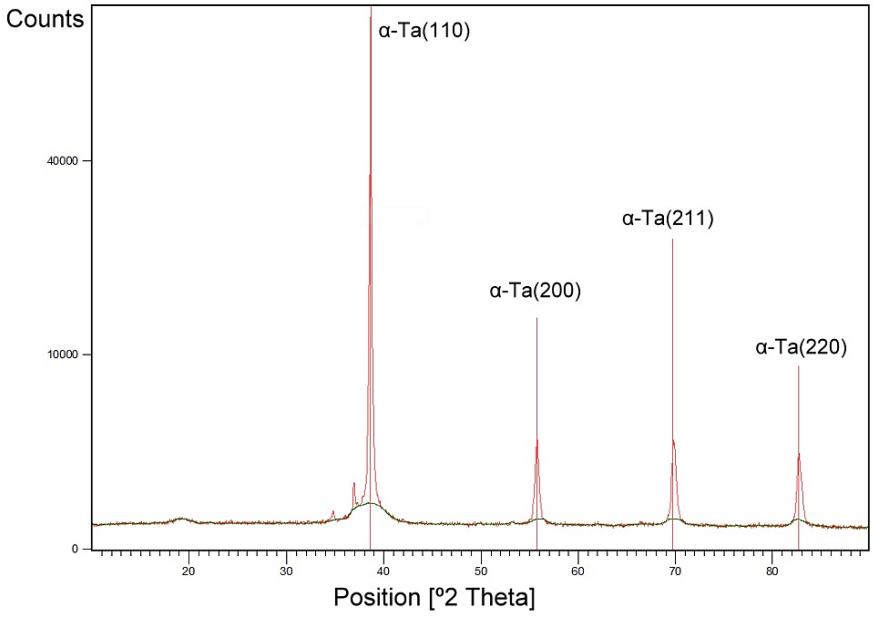

Figure 2. XRD pattern of the as-deposited tantalum. The four peaks centered at 38.66°, 55.75°, 69.81° and 82.68° correspond to (110), (200), (211) and (220) of α-Ta

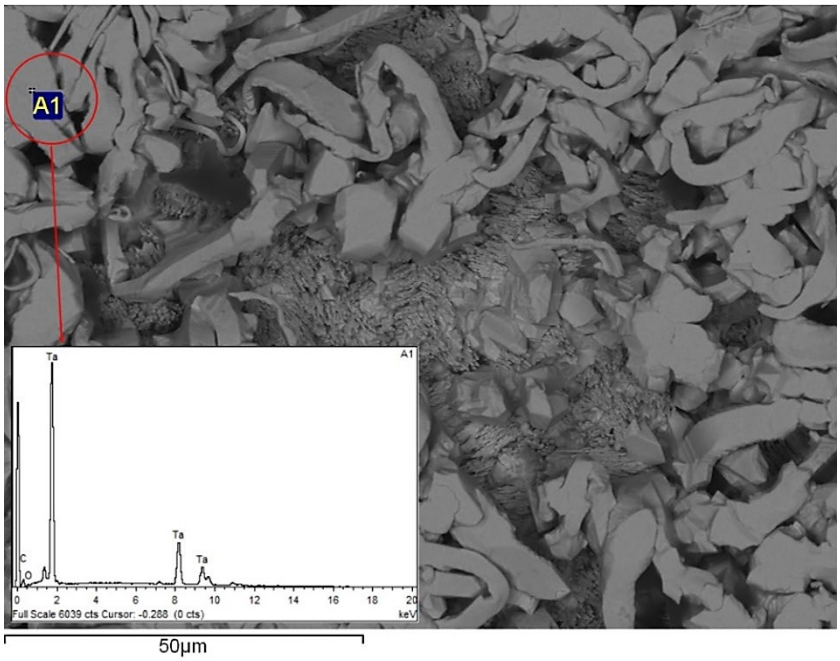

Figure 3. Morphology of the Ta coating as-deposited from a SEM image with the EDX spectrum

The EDX results of the coating surface depicted in Fig. 3 prove the presence of tantalum, as well as carbon and oxygen. Although the oxygen peak is very weak, in the XPS analysis of the Ta coating surface depicted in Fig. 4, both the presence of metallic Ta and Ta oxide in the form of Ta_2O_5 are verified. The Ta 4f core level shows two doublets associated to both the oxidation and metallic state of tantalum. The doublet at the highest binding energy, 26.2/28.1 eV is assigned to Ta(V) in Ta_2O_5 (Ta_{ox}) [47]. The peaks at 21.8 eV (Ta $4f_{7/2}$) and 23.7 eV (Ta $4f_{5/2}$) are associated to metallic tantalum (Ta_{met}) [48]. After removing the organic surface contamination by oxygen plasma, the atomic ratio (in %) of the oxide and metallic species (Ta_{ox}/Ta_{met}) from Fig. 4 for the untreated sample was 4.8. The displacement in the doublet corresponding to the Ta_{met} species is associated to the charge correction applied to the spectrum for the doublet of the Ta_{ox} species, which is non-conductive (the C1s-284.6 eV was used as the reference for the spectrum correction). The sample is slightly insulating due to the presence of the Ta_{ox}, in contrast to the Ta_{met} species, which is conductive. As the signal for both species is detected in the same spectrum, the correction affects both doublets, and the Ta_{met} spectra appear misaligned as a function of the different charge in the samples.

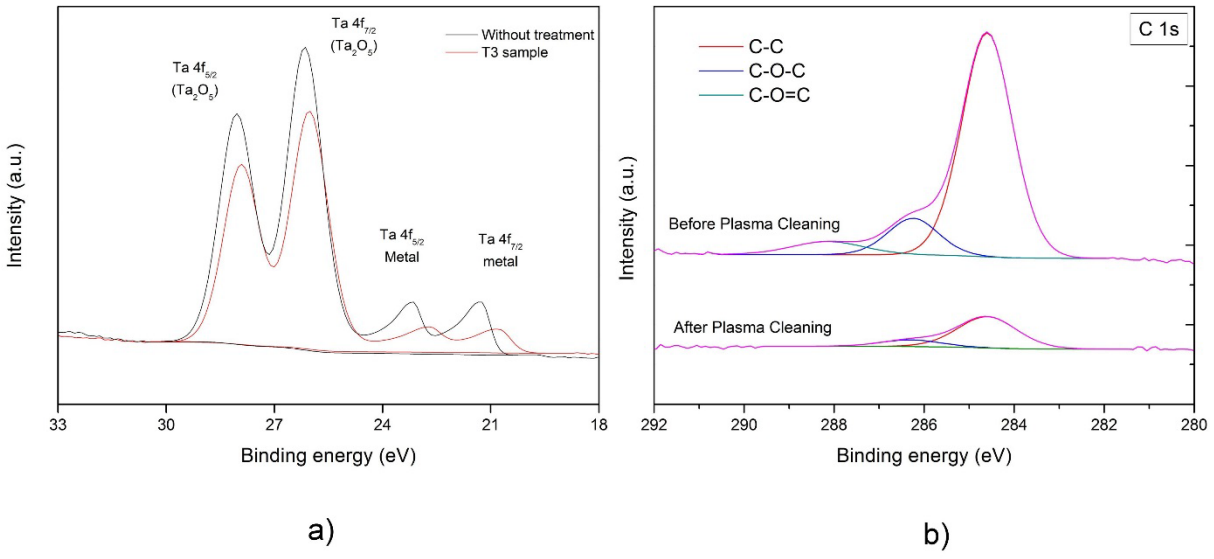

Figure 4. a) High resolution XPS spectra of the Ta 4f core levels for the tantalum coating surface before (black) and after anodic polarization treatment (red; T3 sample). b) Effect of superficial oxygen plasma cleaning on the C 1s spectra (sample without treatment).

3.2. Potentiodynamic polarization

Figure 5 shows the potentiodynamic polarization curves of both the sample T1 and the base metal (AISI 316L SS), obtained according to the DOE specifications for anodic corrosion [33]. Specifically, the voltage range (from −0.4V to +0.6V) was scanned with a sweep rate of 0.1 mV/s. A solution of H_2SO_4 + 0.1 ppm HF with a pH=3 at 80°C, deaerated with N_2 was used as electrolyte

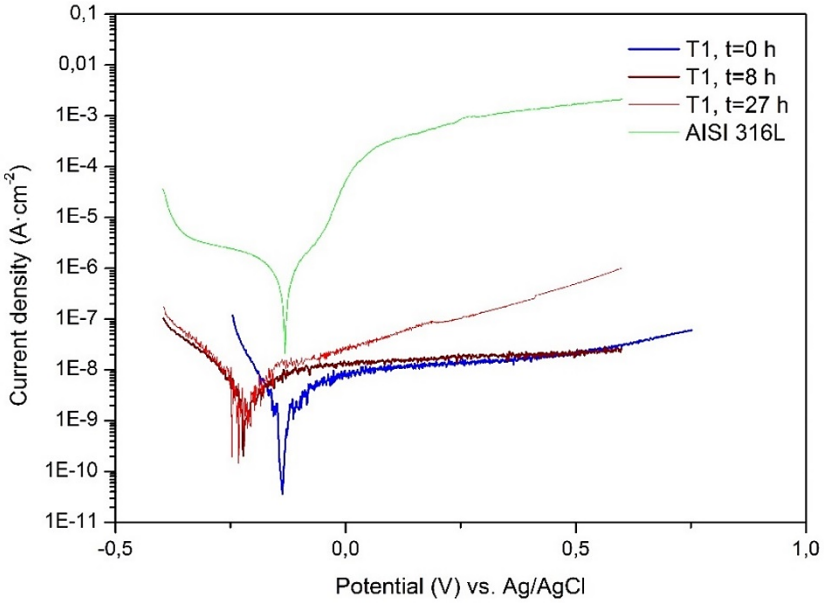

Fig. 5. Potentiodynamic polarization curves of T1 and AISI 316L samples for different polarization times

As can be seen, the Ta coating remarkably improves the properties against corrosion of the AISI 316L SS ($j_{corr\text{-}SS}$: $4x10^{-7}$ A cm^{-2}; $j_{corr\text{-}T1\ 0h}$: $4{,}5x10^{-9}$ A cm^{-2}). After exposing the T1 sample to 27 hours of polarization at +100 mV, the corrosion potential shifts slightly towards negative values, with corrosion current densities ($j_{corr\text{-}T1\ 8h}$: $1.3x10^{-8}$ A cm^{-2}; $j_{corr\text{-}T1\ 27h}$: $3.8x10^{-8}$ Acm^{-2}) always below the target limit established by the DOE (< 10^{-6} A cm^{-2}). After the treatment, transition peaks corresponding to active/passive current density were not observed in the polarization curves.

3.3. Potentiostatic polarization and EIS (T1 and T2)

Figure 6 shows the Nyquist diagrams of sample T1 after being exposed to a polarization of +100 mV for 0, 15 and 27 hours, using a solution of H_2SO_4 + 0.1 ppm HF with a pH=3 at 80°C

as electrolyte, deaerated with N_2. The Nyquist diagram of the AISI 316L SS is also plotted before and after the potentiodynamic polarization (anodic corrosion) similar to the T1 case. It is observed that the Ta coating significantly increases the polarization resistance of the SS, with very high values of the impedance module at low frequencies and absence of capacitive arcs. These results agree with the low current densities obtained in the potentiodynamic polarization tests as discussed in Fig. 5.

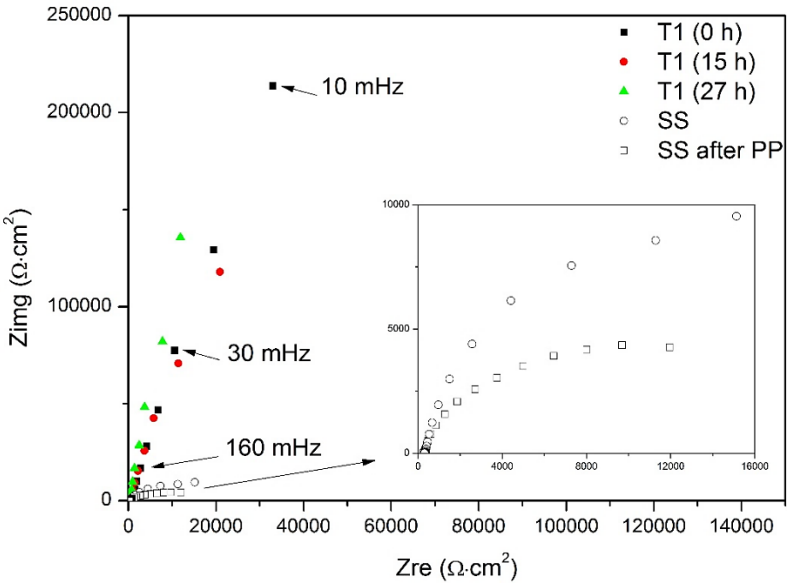

Figure 6. Nyquist impedance diagrams of the T1 and SS samples after a potentiodynamic polarization at 0.1 V for different times. Inset image corresponds to the Nyquist plot of the SS sample

The Nyquist diagrams of sample T2, subjected to potentiostatic polarization tests under cathodic simulated conditions (+600 mV) for a total time of 33 h are shown in Fig. 7. In this case, a solution of H_2SO_4 + 0.1 ppm HF with a pH=3 at 80°C was used as electrolyte, but now saturated with O_2. As can be observed, similar results to the impedance spectra of Fig. 6 (anodic conditions) were obtained. The Ta surface coating does not appear to suffer significant damage for these potentials and treatment times. Therefore, it can be concluded that the Ta-based surface coating provides an adequate protection against corrosion to the AISI 316L SS in both anodic and cathodic operating conditions.

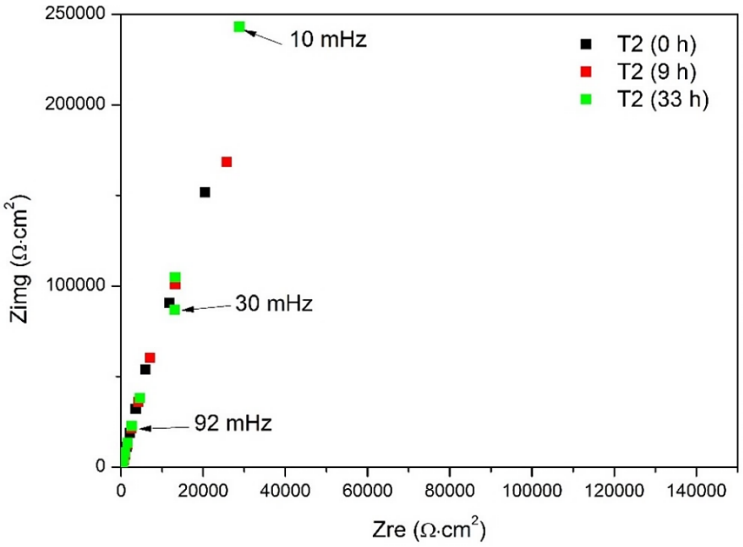

Figure 7. Nyquist impedance diagrams of the T2 samples after a potentiostatic polarization

3.4.- Long-term tests

During the startup and shutdown of a PEMFC, as well as in conditions of hydrogen starvation, bipolar plates can be exposed to high potentials, even higher than 1 V [49], [50], [51]. In order to estimate the durability of the coating at high potentials, long duration tests (> 100 h) were carried out at a potential of 1.139 V. Again, a solution of H_2SO_4 + 0.1 ppm HF with a pH=3 at 80°C, deaerated with O_2, was used as electrolyte. The Nyquist and Bode diagrams obtained for sample T3, for different testing times (209 cycles, corresponding to 104.5 hours of total treatment), are detailed in Fig. 8. It is important to note that after each polarization cycle, and before performing the corresponding impedance test, the potential of the working electrode was stabilized during 15 min.

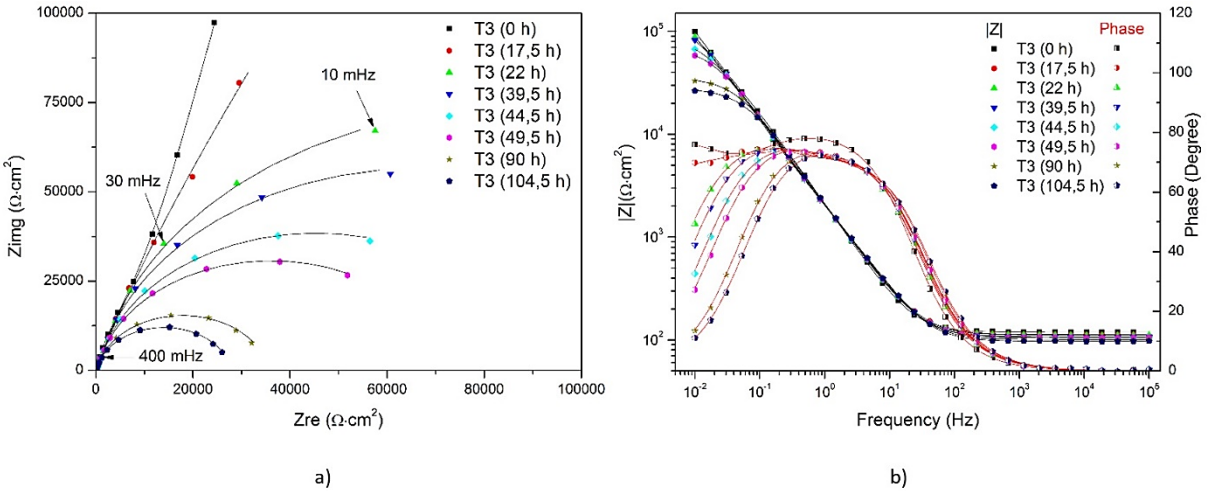

Figure 8. Nyquist (a) and Bode (b) impedance diagrams of the sample T3 after a potentiostatic

polarization at +1.193 V for different times

As can be seen, a qualitative change is observed in the Nyquist diagram after 22 hours of test (Fig. 8a), associated to the appearance of a high frequency capacitive arc, due to the progressive decrease of the protective character of the coating. It agrees with an appreciable change in the current density in the potentiostatic tests, reaching values of 8.02 μA cm^{-2}, which is 8 times higher than the DOE's target (1 μA cm^{-2}). The evolution of the current density reached at the end of the successive treatment cycles is depicted in Fig. 9.

In the Bode diagram of Fig. 8b), it can be observed that as the polarization time increases the modulus of the impedance decreases in the low frequency region, which is associated with low corrosion resistance [52]. So, it has been demonstrated that for this Ta-based coating the protection against corrosion decreases progressively with time, also affecting both the medium and the high phase angle frequency. For this frequency range, a compact and protective coating generally presents values of phase angle close to 90°, indicating a pure capacitive behavior with very good dielectric properties. In this case, the value of the phase angle at high frequencies decreases with time, reaching maxima close to 75°. It is also noted that these maxima extend over a wide range during the frequency sweep of the test, and that it narrows as the time increases due to the degradation of the coating.

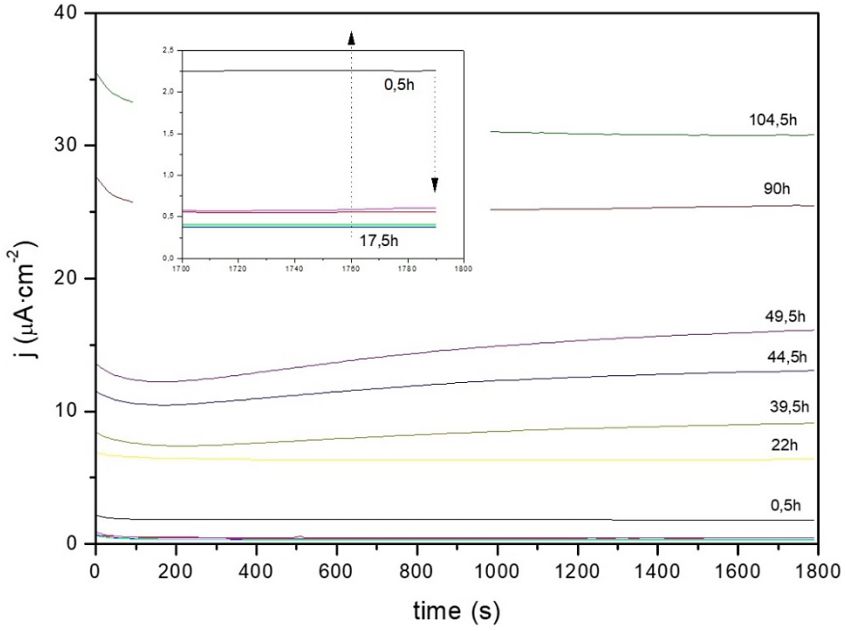

Fig. 9. Current densities for the long-term potentiostatic polarization tests at +1.193 V (30 min cycles) of T2 samples. Electrolyte: H_2SO_4 + 0.1 ppm HF, pH 3, 80°C, O_2 saturated

The time constants associated with an impedance spectrum can be calculated by analyzing

the variation of the phase angle as a function of the frequency in the Bode plot (Fig. 8b). These constants correspond to the maximums of the curve and are associated with their capacitive arcs in the Nyquist diagram in Fig. 8a). Different factors of the metallic coating such as its thickness, porosity, composition, grain size, microstructure and surface morphology, can influence its corrosion resistance to different working environments. These factors are also relevant for choosing the representative equivalent electric circuit and, therefore, to define their associated time constants [53], [54], [55], [56], [57], [58], [59], [60], [61], [62], [63].

In general, the high frequency region of the Bode diagram provides information of the coating defects and changes in the surface area, while the low frequency region is related to the physicochemical phenomena that simultaneously occur at the metal/coating interface [64]. In two-time constants models, the high frequency constant is usually associated with its dielectric properties and resistance to the electrolyte attack in the coating pores, while the low frequency constant is related to the metal corrosion electrochemical reaction and the double layer capacity, which is located at the base metal/coating interface of the micropores [63], [65].

Figure 10 shows the equivalent electrical circuit (EEC) used to adjust the experimental data of the impedance spectra of the Ta coatings. The proposed model contains two time constants. The half-frequency constant is associated to the coating, while the low-frequency one corresponds to the resistance of the charge transfer process at the metal/coating interface. The resistance of the electrolyte, R_1, is connected in series with the rest of the elements in the circuit. The values of R_3/CPE_3 agree with both the resistance to the charge transfer process and the non-ideal capacity of the double layer, while R_2/CPE_2 is associated with the resistance and non-ideal capacity of the coating micropores. In the CPE_2 element, a parallel resistance is not considered because it is assumed that it is very high and can be eliminated from the model [66]. Furthermore, at the base of the micropores, the capacity of both the oxide covering the stainless steel and the Ta-oxide of the coating, arranged in parallel, could be assumed to be equal, so that only a single element CPE_2 is used [63]. R_2 corresponds to the micropores coating resistance to the electrolyte attack.

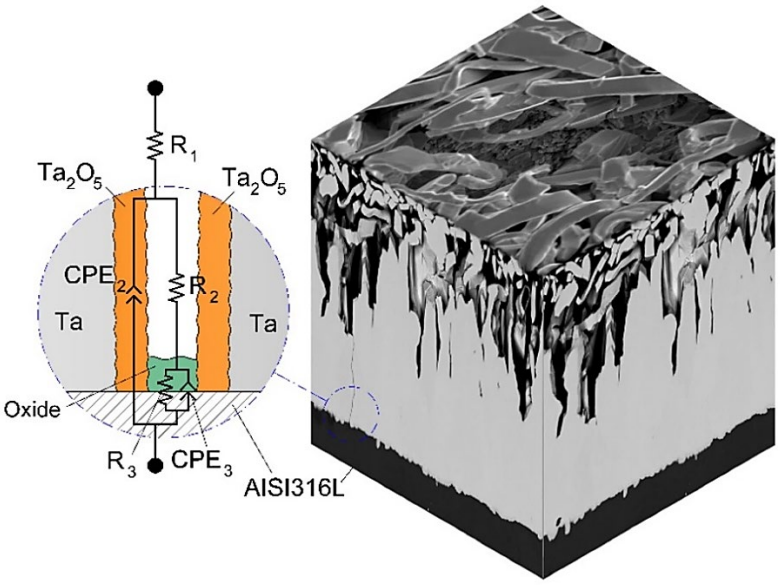

Fig. 10. Equivalent circuit model used for the fitting of EIS results for Ta coatings

The constant phase element, CPE, can be used to simulate the non-ideal behavior of a capacitor [63]. CPE could be defined by two values, CPE-T(T) and CPE-P(P). The CPE impedance is defined as [65]:

$$Z_{CEP} = \frac{1}{[T(j\,w)^P]} \tag{2}$$

where $j = \sqrt{-1}$, $w = 2\pi\, f$ is the angular frequency (rad/s), and f is the frequency (Hz). P is a dimensionless number related to non-uniform current distributions due to roughness and surface inhomogeneity, and varies between 0 and 1. CPE becomes a resistance when P = 0, a Warburg element when P = 0.5 (semi-infinite length diffusion phenomena), and an ideal capacitor when P = 1. The fitting parameters T, P and R of each R/CPE pair can be used to calculate capacities from the equation [67], [68], [69],

$$C = R^{[(1-P)/P]}T^{1/P} \tag{3}$$

The experimental values of CPE_2-P are in the range 0.79–0.91, slightly different from the ideal capacitive behavior (associated with the coating surface roughness), while the value of CPE_3-P have a purely capacitive character. In the case of TaN coatings on stainless steel values very close to unity are also obtained for this parameter [63].

Table 1 shows the values fitted for the EEC elements. C_2 values, calculated from the fitted data of CPE_2 and Eq. (3), decrease for increasing time, ranging from an initial value of 109 μF down to 68.7 μF when the treatment is finished (104.5 h). For this capacity, C_2, an average value of 89.39 μF is obtained.

Table 1. Electrical parameters, and resulting χ^2 values obtained by CNLS fitings of ECC in Figure 14 for the impedance spectra of T2 samples shown in Figure 12

t	0	22	39.5	49.5	90	104.5
R_1 [Ω cm^2]	118.6	111.4	106.6	105.1	101.1	96.92
CPE_2-T [S^p/Ω cm^2]	$8.91x10^{-5}$	$9.32x10^{-5}$	$8.93x10^{-5}$	$8.56x10^{-5}$	$7.83x10^{-5}$	$7.77x10^{-5}$
CPE_2-P	0.912	0.882	0.884	0.888	0.897	0.898
R_2 [Ω cm^2]	87684	18988	13469	9106	5312	4320
CPE_3-T [S^p/Ω cm^2]	$3.62x10^{-5}$	$2.04x10^{-5}$	$1.90x10^{-5}$	$1.66x10^{-5}$	$1.67x10^{-5}$	$1.68x10^{-5}$
CPE_3-P	0.866	1	1	1	0.997	0.985
R_3 [Ω cm^2]	$8.62x10^{6}$	155200	119890	62959	30249	23534
χ^2	$5.48x10^{-4}$	$1.04x10^{-3}$	$1.17x10^{-3}$	$7.28x10^{-4}$	$8.95x10^{-4}$	$7.96x10^{-4}$
C_2 [F cm^{-2}]	$1.09x10^{-4}$	$1.01x10^{-4}$	$9.15x10^{-5}$	$8.30x10^{-5}$	$7.08x10^{-5}$	$6.87x10^{-5}$
C_3 [F cm^{-2}]	$8.81x10^{-5}$	$2.04x10^{-5}$	$1.90x10^{-5}$	$1.66x10^{-5}$	$1.67x10^{-5}$	$1.66x10^{-5}$

The anodic oxidation of Ta coating in acidic solutions leads to the formation of Ta_2O_5 [44], [70]. The corresponding cathodic half-reaction is [71], [72]:

$$Ta_2O_5 + 10H^+ + 10\,e^- \rightleftharpoons 2\,Ta + 5\,H_2O\,, \qquad E^0 = 0.75\,V\ vs.SHE \tag{4}$$

The formation of Ta_2O_5 is an irreversible process that produces an amorphous, passive and compact oxide [71]. Its physicochemical properties are very different depending on the concentration of the electrolyte used [73]. In addition, the Ta substrates from which Ta_2O_5 is formed can present a native TaO layer, which influences the dielectric properties when the layer thickness exceeds 19 nm [71]. The incorporation of the anions of the electrolyte in the oxide layer of Ta_2O_5 increases its resistivity in concentrated solutions of H_2SO_4 (95%), reducing its dielectric constant. Its composition can be represented by $Ta_2O_{5(1-x)}(SO_4)_{5x}$, where x is 0.27 and 0.30 respectively, and it is formed by a single oxide layer doped with SO_4^{2-} anions. However, in dilute acid solutions (0.1 M) the oxide has a double layer structure, with an internal layer of Ta_2O_5 strongly adhered to the substrate, and an external layer doped with SO_4^{2-} anions.

The EDX analysis of the Ta-coated surface after the anodic polarization does not show the presence of sulfur, which would be associated to the incorporation of SO_4^{2-} in the oxide layer. This fact would be favored by the low concentration of electrolyte used (10^{-3} M H_2SO_4) to simulate the cathode operating environment during the cathodic polarization test.

Although the superficial Ta oxide produced when anodizing is formed by a multilayer structure, such elements would be indistinguishable and characterized by a single value of C_2 (Table 1). On the other hand, it is important to note that the capacity of the anodic Ta_2O_5 is independent of the applied potential for thicknesses above 15 nm [72]. To reach this

thickness, high potentials or current densities have to be applied to the Ta coating surface. When using H_2SO_4 as the electrolyte, the anodizing coefficient is 1.54 ± 0.04 nm V^{-1} [70]. As in this study the maximum anodization potential was 1.193 V, the thickness of the surface oxide of the coating is probably of only a few nanometers. On the other hand, the dielectric properties of Ta_2O_5 depend on both the layer thickness and the nature (amorphous or crystalline) of the oxide. The dielectric constant reached values up to 60 for crystalline Ta_2O_5 on Si substrates, which is mainly influenced by the presence of the native TaO layer and the characteristics of the substrate on which it is deposited [74]. The presence of metallic particles of Ta in an amorphous matrix of Ta_2O_5 is also responsible for the deviation (increase) in the dielectric constant value from the one theoretically predicted [75]. The atomic ratio (in %) of 4.8 for the oxide and metallic species (Ta_{ox}/Ta_{met}) obtained by XPS for a non-polarized Ta coating, is increased to 6.23 for the sample exposed above 100 hours to an anodic polarization of 1.193 V. Considering the experimental conditions (anodized coefficient and maximum potential) used during the tests, the increase verified for the Ta_{ox}/Ta_{met} ratio is not very relevant, as expected. The presence of Ta_{met} and C detected by XPS could therefore be responsible for the high value of C_2 obtained when adjusting the model for the EEC.

The capacity corresponding to an oxide layer can be expressed as [74]:

$$C = \frac{\varepsilon \varepsilon_o}{\delta} \tag{5}$$

where ε_o is the vacuum permittivity ($\varepsilon_o = 8{,}885 \times 10^{-12}$ F m^{-1}), ε is the dielectric constant of the material, and δ the thickness of the oxide layer. Since the C_2 value characterizes the thickness of the surface oxide layer, results obtained indicate that it increases progressively with the number of polarization cycles applied at 1.193 V, causing a decrease in the total capacity. This behavior is observed in the values of C_2 of Table 1 although, as previously discussed, it is not really significant.

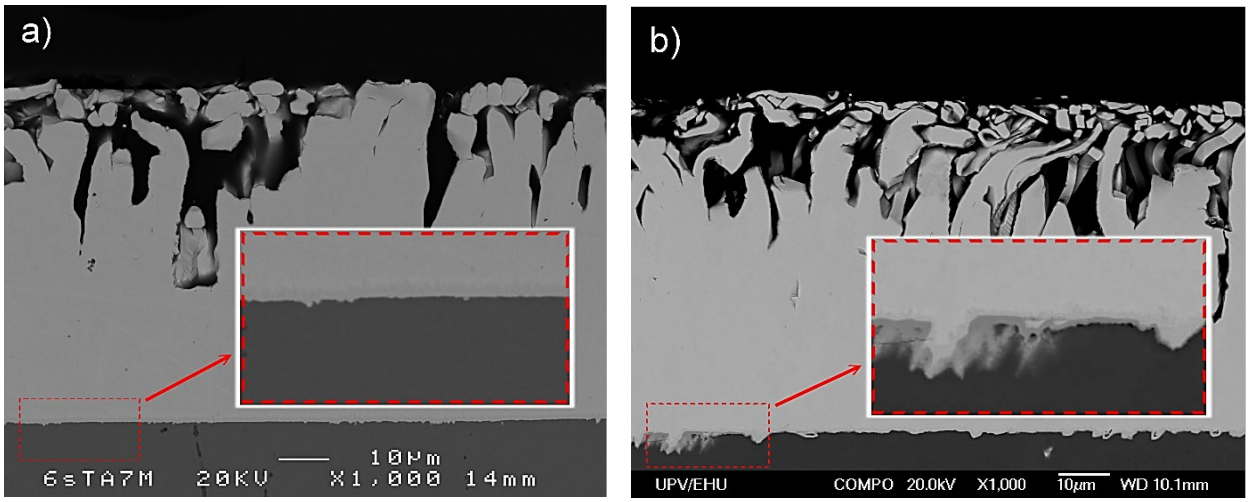

Figure 11. Coating cross-section SEM images of T2 samples before(a) and after (b) potentiostatic polarization tests

Finally, the total polarization resistance of the sample (R_2+R_3) decreases with anodizing time, as predicted by the proposed model, indicating the progressive coating degradation. For coatings with a columnar growth morphology, the particles deposited on the substrate grow and collapse forming a dense and continuous deposit. In Ni(P) coatings, for example, the preferred locations for the electrolyte penetration toward the metal/coating interface are just the inter-columnar interfaces. This process eventually causes the delamination favored by the galvanic corrosion [54], [76]. The SEM image of Fig. 1a) shows a dense coating with micropores as a result of the imperfect compaction during the columnar growth of the α-Ta crystals. After the potentiostatic polarization, no superficial morphological changes are observed, as can be seen in Fig. 11. On the contrary, small modifications in the metal/coating interface are observed associated to less dense areas with small pores, probably due to localized corrosion caused by the penetration of the electrolyte to the interface through the pore network. Delamination processes at the metal/coating interface are not observed. Straight paths for the electrolyte penetration to the base metal are not formed, improving the overall coating protection.

3.5.- Interfacial contact resistance (ICR)

The first interesting result is that ICR values obtained for pre- and post-polarization tests are very similar, in the range of 22.3 to 32.6 mΩ cm^2 for a clamping pressure of 140 N cm^{-2}. As expected, the ICR decreases when the compaction pressure is increased [77], and the dispersion detected for the experimental data is probably due to the rough nature of the

coating surface, as evidenced in the SEM images of Figs. 1 and 11. These values are lower than those obtained for coatings of Ta on 430 SS (154.5 – 192 mΩ cm^2) [30] or for metallic Ta or TaN coatings on SS316L (82 mΩ cm^2 and 362 – 538 mΩ cm^2, respectively) for similar clamping pressures [29].

Surface contact resistance of metallic materials is governed by both the surface morphology and the electrical properties of the oxides generated over the surface by the corrosion processes. The capacity C_2 associated with the surface oxide obtained from the model fitted to the EIS data remains almost constant with the anodizing process. Besides, the chemical composition of the surface oxide does not change either, except for the slight increase in the Ta_{ox}/Ta_{met} ratio already discussed. Therefore, it seems that the influence of the anodizing processes on the ICR values can be neglected.

3.6.- Hydrophobic properties

Hydrophobic properties of coatings mainly depend on the chemical composition and roughness of the surface [78]. Figure 12 shows images of the contact angle before and after the corrosion tests for samples T1 and T2. It is observed that the contact angle is above 95°, meaning that the coatings have very good hydrophobic properties, slightly increasing the initial values. In addition, the surface roughness values (0.6–0.7 μm) barely change after the polarization cycles. Results obtained confirm the hydrophobic character of the coating, with a slight increase in the contact angle values after the anodizing processes.

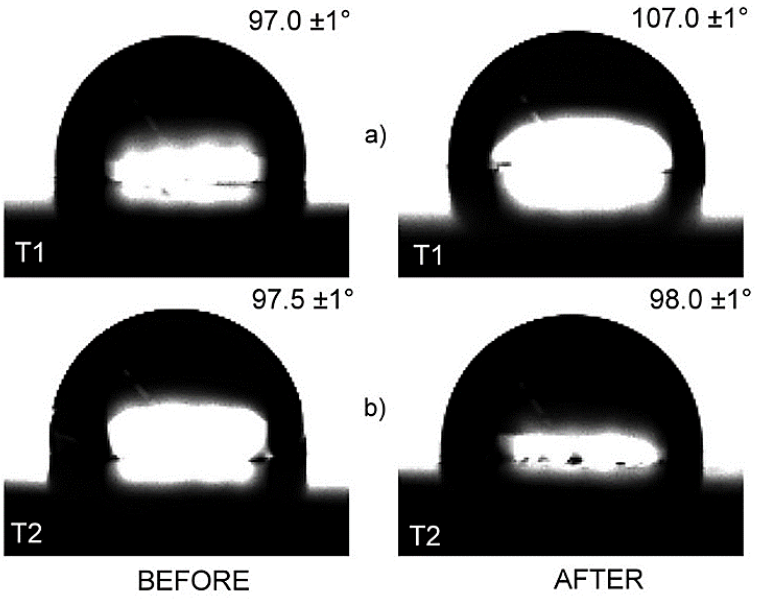

Figure 12. Contact angle images of T1 (a) and T2 (b) samples before and after the corrosion tests

4.- Conclusions

The behavior against corrosion of Ta-based coatings of 30 μm thickness deposited by CVD on AISI 316L SS has been studied in detail. Results obtained from EIS, potentiodynamic, and potentiostatic polarization tests reveal the excellent protection against corrosion provided by these coatings for the simulated anodic and cathodic conditions typically occurring in PEMFCs. After the long-term polarization tests, SEM images show a compact surface Ta coating with the existence of small pores. However, as cracking straight paths are not formed, the coating acts as an efficient protection to the base metal for the electrolyte attack.

No morphological changes, loss of coating adherence or a decrease in its excellent hydrophobic properties (contact angle above 95°) were observed during the long-term polarization tests. It was also found that the polarization treatment does not produce substantial changes in either roughness or ICR values. The anodizing process produces a protective surface film formed by Ta oxide in the form of Ta_2O_5, coexisting with metallic Ta specie (α-Ta, bbc), with a Ta_{ox}/Ta_{met} atomic ratio slightly increasing from 4.8 to 6.23 after the polarization tests, and some carbon from residual contamination. This combination of elements produces a coating capacity higher than that of the pure Ta_2O_5, of marked dielectric character, improving the electrical conduction properties of the coating. The performance of the Ta-based coatings under both anodic and cathodic operating conditions suggests that PEMFC stacks formed by very thin stainless steel bipolar plates coated with tantalum will have an excellent performance and a large lifetime.

Acknowledgments

Authors acknowledge the financial support of the Secretariat of State for Research of the Spanish Ministry of Economy and Competitiveness under project DPI2015-69286-C3-1-R, and the Spanish Ministry of Science, Innovation and Universities under the project RTI2018-096001-B-C31. Support of the Regional Government of Aragon to the Fluid Mechanics for a Clean Energy Research Group (T01_17R) of the LIFTEC is also acknowledged, as well as the technical and human support of the Materials and Surfaces Service provided by SGIker (UPV/EHU/ ERDF, EU).

References

[1] Olabi AG, Ijaodola O, Hassan Z El, Thompson J, Ogungbemi E, Wilberforce T. Effect of Bipolar Plate Materials on Performance of Fuel Cells. Ref. Modul. Mater. Sci. Mater. Eng., Elsevier; 2018. doi:10.1016/b978-0-12-803581-8.11272-x.

[2] Spendelow J, Marcinkoski J. DOE Hydrogen and Fuel Cells Program Record -2011 2011; 2: 1–4.

[3] André J, Antoni L, Petit JP. Corrosion resistance of stainless steel bipolar plates in a PEFC environment: A comprehensive study. Int J Hydrogen Energy 2010; 35: 3684–97. doi:10.1016/j.ijhydene.2010.01.062.

[4] Hermann A, Chaudhuri T, Spagnol P. Bipolar plates for PEM fuel cells: A review. Int J Hydrogen Energy 2005; 30: 1297–302. doi:10.1016/j.ijhydene.2005.04.016.

[5] Tawfik H, Hung Y, Mahajan D. Metal bipolar plates for PEM fuel cell-A review. J Power Sources 2007; 163:755–67. doi:10.1016/j.jpowsour.2006.09.088.

[6] Dihrab SS, Sopian K, Alghoul MA, Sulaiman MY. Review of the membrane and bipolar plates materials for conventional and unitized regenerative fuel cells. Renew Sustain Energy Rev 2009; 13: 1663–8. doi:10.1016/j.rser.2008.09.029.

[7] Antunes RA, De Oliveira MCL, Ett G, Ett V. Carbon materials in composite bipolar plates for polymer electrolyte membrane fuel cells: A review of the main challenges to improve electrical performance. J Power Sources 2011; 196: 2945–61. doi:10.1016/j.jpowsour.2010.12.041.

[8] Karimi S, Fraser N, Roberts B, Foulkes FR. A Review of Metallic Bipolar Plates for Proton Exchange Membrane Fuel Cells: Materials and Fabrication Methods. Adv Mater Sci Eng 2012; 2012: 1–22. doi:10.1155/2012/828070.

[9] De Oliveira MCL, Ett G, Antunes RA. Materials selection for bipolar plates for polymer electrolyte membrane fuel cells using the Ashby approach. J Power Sources 2012; 206: 3–13. doi:10.1016/j.jpowsour.2012.01.104.

[10] Taherian R. A review of composite and metallic bipolar plates in proton exchange membrane fuel cell: Materials, fabrication, and material selection. J Power Sources 2014; 265: 370–90. doi:10.1016/j.jpowsour.2014.04.081.

[11] Iwan A, Malinowski M, Pasciak G. Polymer fuel cell components modified by graphene: Electrodes, electrolytes and bipolar plates. Renew Sustain Energy Rev 2015; 49: 954–67. doi:10.1016/j.rser.2015.04.093.

[12] Peng L, Yi P, Lai X. Design and manufacturing of stainless steel bipolar plates for proton exchange membrane fuel cells. Int J Hydrogen Energy 2014; 39: 21127–53. doi:10.1016/j.ijhydene.2014.08.113.

[13] Antunes RA, Oliveira MCL, Ett G, Ett V. Corrosion of metal bipolar plates for PEM fuel cells: A review. Int J Hydrogen Energy 2010; 35: 3632–47. doi:10.1016/j.ijhydene.2010.01.059.

[14] Feng K, Shen Y, Mai J, Liu D, Cai X. An investigation into nickel implanted 316L stainless steel as a bipolar plate for PEM fuel cell. J Power Sources 2008; 182: 145–52. doi:10.1016/j.jpowsour.2008.03.088.

[15] Chu PK, Liu D, Cai X, Shen Y, Feng K. Ni–Cr Co-implanted 316L stainless steel as bipolar plate in polymer electrolyte membrane fuel cells. Int J Hydrogen Energy 2009; 35: 690–700. doi:10.1016/j.ijhydene.2009.10.106.

[16] Abreu CM, Cristóbal MJ, Merino P, Nóvoa XR, Pena G, Pérez MC. Electrochemical behaviour of an AISI 304L stainless steel implanted with nitrogen. Electrochim Acta 2008; 53: 6000–7. doi:10.1016/j.electacta.2008.03.064.

[17] Abreu CM, Cristóbal MJ, Figueroa R, Nóvoa XR, Pena G. Evolution of corrosion behavior for AA7075 aluminum alloy implanted with nitrogen. Nucl Instruments Methods Phys Res Sect B Beam Interact with Mater Atoms 2019; 442: 1–12. doi:10.1016/j.nimb.2019.01.013.

[18] Feng K, Li Z, Cai X, Chu PK. Silver implanted 316L stainless steel as bipolar plates in polymer electrolyte membrane fuel cells. Mater Chem Phys 2011; 126: 6–11. doi:10.1016/j.matchemphys.2010.11.029.

[19] Huang N, Liang C, Wang H, Xu L, Xu H. Corrosion behavior of passivated 316LSS with Ag coating as PEMFC bipolar plate. Int J Corros 2011; 2011. doi:10.1155/2011/103785.

[20] Jin J, Zheng D, Liu H. The corrosion behavior and mechanical properties of CrN/Ni-P multilayer coated mild steel as bipolar plates for proton exchange membrane fuel cells. Int J Hydrogen Energy 2017; 42: 28883–97. doi:10.1016/j.ijhydene.2017.10.046.

[21] Asri NF, Majlan EH, Husaini T, Daud WRW, Sulong AB. Coating of stainless steel and titanium bipolar plates for anticorrosion in PEMFC: A review. Int J Hydrogen Energy 2016; 42: 9135–48. doi:10.1016/j.ijhydene.2016.06.241.

[22] Gao P, Xie Z, Wu X, Ouyang C, Lei T, Yang P, et al. Development of Ti bipolar plates with carbon/PTFE/TiN composites coating for PEMFCs. Int J Hydrogen Energy 2018; 43:

20947–58. doi:10.1016/j.ijhydene.2018.09.046.

[23] Barranco J, Barreras F, Lozano A, Lopez AM, Roda V, Martin J, Maza M, Fuentes GG, Almandoz E. Cr and Zr/Cr nitride CAE-PVD coated aluminum bipolar plates for polymer electrolyte membrane fuel cells. Int J Hydrogen Energy 2010; 35: 11489–98. doi:10.1016/j.ijhydene.2010.05.050.

[24] Chanda UK, Behera A, Roy S, Pati S. Evaluation of Ni-Cr-P coatings electrodeposited on low carbon steel bipolar plates for polymer electrolyte membrane fuel cell. Int J Hydrogen Energy 2018; 43: 23430–40. doi:10.1016/j.ijhydene.2018.10.218.

[25] Barranco J, Barreras F, Lozano A, Maza M. Influence of CrN-coating thickness on the corrosion resistance behaviour of aluminium-based bipolar plates. J Power Sources 2011; 196: 4283-9. doi:10.1016/j.jpowsour.2010.11.069

[26] Yu H, Yang L, Zhu L, Jian X, Wang Z, Jiang L. Anticorrosion properties of Ta-coated 316L stainless steel as bipolar plate material in proton exchange membrane fuel cells. J Power Sources 2009; 191: 495–500. doi:10.1016/j.jpowsour.2009.02.020.

[27] Choe C, Choi H, Hong W, Lee JJ. Tantalum nitride coated AISI 316L as bipolar plate for polymer electrolyte membrane fuel cell. Int J Hydrogen Energy 2012; 37: 405–11. doi:10.1016/j.ijhydene.2011.09.060.

[28] Alishahi M, Mahboubi F, Mousavi Khoie SM, Aparicio M, Hübner R, Soldera F, et al. Electrochemical behavior of nanocrystalline Ta/TaN multilayer on 316L stainless steel: Novel bipolar plates for proton exchange membrane fuel-cells. J Power Sources 2016; 322: 1–9. doi:10.1016/j.jpowsour.2016.04.133.

[29] Mendizabal L, Oedegaard A, Kongstein OE, Lædre S, Walmsley J, Barriga J, et al. TaN_X coatings deposited by HPPMS on SS316L bipolar plates for polymer electrolyte membrane fuel cells: Correlation between corrosion current, contact resistance and barrier oxide film formation. Int J Hydrogen Energy 2017; 42: 3259–70. doi:10.1016/j.ijhydene.2017.01.070.

[30] Wang L, Li L, Liu H, Wang S, Fang H, Gao H, et al. Polylaminate TaN/Ta coating modified ferritic stainless steel bipolar plate for high temperature proton exchange membrane fuel cell. J Power Sources 2018; 399: 343–9. doi:10.1016/j.jpowsour.2018.07.122.

[31] Nikiforov A V., Petrushina IM, Christensen E, Tomás-García AL, Bjerrum NJ. Corrosion behaviour of construction materials for high temperature steam electrolysers. Int J Hydrogen Energy 2011;36: 111–9. doi:10.1016/j.ijhydene.2010.09.023.

[32] Jensen AH, Christensen E, von Barner JH. Contact Resistance of Tantalum Coatings in Fuel Cells and Electrolyzers Using Acidic Electrolytes at Elevated Temperatures. ECS Electrochem Lett 2014; 3: F50–1. doi:10.1149/2.0051407eel.

[33] Sciences C, Division E. 2017 Bipolar Plate Workshop Report 2017.

[34] BioLogic Science Instruments. Equivalent model of an electrochemical cell including the reference electrode impedance and the potentiostat parasitics 2013: 1–6. doi:http://dx.doi.org/10.1007/s10519-015-9742-6.

[35] Princeton Applied Research. Best Practices for Improving Tafel Plots of High Capacitance Cells with Low Series Resistance 2014.

[36] Tran AT, Huet F, Ngo K, Rousseau P. Artefacts in electrochemical impedance measurement in electrolytic solutions due to the reference electrode. Electrochim Acta 2011; 56: 8034–9. doi:10.1016/j.electacta.2010.12.088.

[37] Borup R, Mukundan R, Lanl TR, Brady M, Ornl JT, Papadias DD, et al. (Metal) Bipolar Plate Testing DOE 2017 Bipolar Plates Workshop 2017.

[38] Hinds G, Brightman E. In situ mapping of electrode potential in a PEM fuel cell. Electrochem Commun 2012; 17: 26–9. doi:10.1016/j.elecom.2012.01.007.

[39] Sasaki K., Shao M., Adzic R. (2009) Dissolution and Stabilization of Platinum in Oxygen Cathodes. In: Büchi F.N., Inaba M., Schmidt T.J. (eds) Polymer Electrolyte Fuel Cell Durability. Springer, New York, NY. doi:10.1007/978-0-387-85536-3_2.

[40] URL: https://www.iam.kit.edu/wet/english/Lin-KK.php [Consulted: 27 may 2019]

[41] Schönleber M, Klotz D, Ivers-Tiffée E. A Method for Improving the Robustness of linear Kramers-Kronig Validity Tests. Electrochim Acta 2014; 131: 20–7. doi:10.1016/j.electacta.2014.01.034.

[42] Boukamp BA. A Linear Kronig-Kramers Transform Test for Immittance Data Validation. J Electrochem Soc 1995; 142: 1885–901. doi:10.1149/1.2044210.

[43] Papadias DD, Ahluwalia RK, Thomson JK, Meyer HM, Brady MP, Wang H, et al. Degradation of SS316L bipolar plates in simulated fuel cell environment: Corrosion rate, barrier film formation kinetics and contact resistance. J Power Sources 2015; 273: 1237–49. doi:10.1016/j.jpowsour.2014.02.053.

[44] Wang L, Li L, Shen J, Gao H, Sun J, Wang H, et al. High conductivity and anti-corrosive tantalum surface modified ferritic stainless steel bipolar plate for direct ethanol fuel cell. Results Phys 2019; 14: 102394. doi:10.1016/j.rinp.2019.102394.

[45] Lee YJ, Lee TH, Kim DY, Nersisyan HH, Han MH, Kang KS, et al. Microstructural and corrosion characteristics of tantalum coatings prepared by molten salt electrodeposition. Surf Coatings Technol 2013; 235: 819–26. doi:10.1016/j.surfcoat.2013.09.007.

[46] Yuan ZL, Zhang DH, Li CY, Prasad K, Tan CM, Tang LJ. A new method for deposition of cubic Ta diffusion barrier for Cu metallization. Thin Solid Films 2003; 434: 126–9. doi:10.1016/S0040-6090(03)00532-7.

[47] Díaz B, Światowska J, Maurice V, Pisarek M, Seyeux A, Zanna S, et al. Chromium and tantalum oxide nanocoatings prepared by filtered cathodic arc deposition for corrosion protection of carbon steel. Surf Coatings Technol 2012;206:3903–10. doi:10.1016/j.surfcoat.2012.03.048.

[48] Brumbach MT, Mickel PR, Lohn AJ, Mirabal AJ, Kalan MA, Stevens JE, et al. Evaluating tantalum oxide stoichiometry and oxidation states for optimal memristor performance. J Vac Sci Technol A Vacuum, Surfaces, Film 2014; 32: 051403. doi:10.1116/1.4893929.

[49] Polymer Electrolyte Fuel Cell Durability, Felix N. Büchi , Minoru Inaba, Thomas J. Schmidt Editors, doi:10.1007/978-0-387-85536-3, Springer Science+Business Media, LLC 2009.

[50] Alegre C, Álvarez-Manuel L, Mustata R, Valiño L, Lozano A, Barreras F. Assessment of the durability of low-cost Al bipolar plates for High Temperature PEM Fuel Cells. Int J Hydrogen Energy 2019; 44: 12748-59. doi:10.1016/j.ijhydene.2018.07.070

[51] Alegre C, Lozano A, Pérez Manso A, Álvarez-Manuel L, Fernández F, Barreras F. Single cell induced starvation in a high temperature proton exchange membrane fuel cell stack. App Energy 2019; 250: 1176-89. doi:10.1016/j.apenergy.2019.05.061

[52] Winiarski J, Gałuszka M, Stankiewicz A. Corrosion resistance of Ni-P\$CePO_4$ coatings obtained from sol solutions. Mater Corros 2015; 66: 557–61. doi:10.1002/maco.201307570.

[53] Özkan S, Hapçi G, Orhan G, Kazmanli K. Electrodeposited Ni/SiC nanocomposite coatings and evaluation of wear and corrosion properties. Surf Coatings Technol 2013; 232: 734–41. doi:10.1016/j.surfcoat.2013.06.089.

[54] Ashassi-Sorkhabi H, Es'haghi M. Corrosion resistance enhancement of electroless Ni-P coating by incorporation of ultrasonically dispersed diamond nanoparticles. Corros Sci

2013; 77: 185–93. doi:10.1016/j.corsci.2013.07.046.

[55] Beliardouh NE, Bouzid K, Nouveau C, Tlili B, Walock MJ. Tribological and electrochemical performances of Cr/CrN and Cr/CrN/CrAlN multilayer coatings deposited by RF magnetron sputtering. Tribol Int 2015; 82: 443–52. doi:10.1016/j.triboint.2014.03.018.

[56] Lee JH, Ahn SH, Kim JG. Effect of Al additions in WC-($Cr_{1-x}Al_x$)N coatings on the corrosion resistance of coated AISI D2 steel in a deaerated 3.5 wt.% NaCl solution. Surf Coatings Technol 2005; 190: 417–27. doi:10.1016/j.surfcoat.2004.03.054.

[57] Chipatecua YL, Olaya JJ, Arias DF. Corrosion behaviour of CrN/Cr multilayers on stainless steel deposited by unbalanced magnetron sputtering. Vacuum 2012; 86: 1393–401. doi:10.1016/j.vacuum.2012.01.016.

[58] Liu L, Xu J, Xie ZH, Munroe P. The roles of passive layers in regulating the electrochemical behavior of Ti_5Si_3-based nanocomposite films. J Mater Chem A 2013; 1: 2064–78. doi:10.1039/c2ta00510g.

[59] Gao R, Du M, Sun X, Pu Y. Study of the corrosion resistance of electroless Ni-P deposits in a sodium chloride medium. J Ocean Univ China 2007; 6: 349–54. doi:10.1007/s11802-007-0349-2.

[60] Liu C, Bi Q, Matthews A. EIS comparison on corrosion performance of PVD TiN and CrN coated mild steel in 0.5 N NaCl aqueous solution. Corros Sci 2001; 43: 1953–61. doi:10.1016/S0010-938X(00)00188-8.

[61] Liu C, Bi Q, Leyland A, Matthews A. An electrochemical impedance spectroscopy study of the corrosion behaviour of PVD coated steels in 0.5 N NaCl aqueous solution: Part I. Establishment of equivalent circuits for EIS data modelling. Corros Sci 2003; 45: 1243–56. doi:10.1016/s0010-938x(02)00213-5.

[62] Pech D, Steyer P, Loir AS, Sánchez-López JC, Millet JP. Analysis of the corrosion protective ability of PACVD silica-based coatings deposited on steel. Surf Coatings Technol 2006; 201: 347–52. doi:10.1016/j.surfcoat.2005.11.130.

[63] Alishahi M, Mahboubi F, Mousavi Khoie SM, Aparicio M, Lopez-Elvira E, Méndez J, et al. Structural properties and corrosion resistance of tantalum nitride coatings produced by reactive DC magnetron sputtering. RSC Adv 2016; 6: 89061–72. doi:10.1039/c6ra17869c.

[64] Contreras A, León C, Jimenez O, Sosa E, Pérez R. Electrochemical behavior and

microstructural characterization of 1026 Ni-B coated steel. Appl Surf Sci 2006; 253: 592–9. doi:10.1016/j.apsusc.2005.12.161.

[65] Galván JC, Larrea MT, Braceras I, Multigner M, González-Carrasco JL. In vitro corrosion behaviour of surgical 316LVM stainless steel modified by Si + ion implantation - An electrochemical impedance spectroscopy study. J Alloys Compd 2016; 676: 414–27. doi:10.1016/j.jallcom.2016.03.162.

[66] Zeng A, Liu E, Annergren IF, Tan SN, Zhang S, Hing P, et al. EIS capacitance diagnosis of nanoporosity effect on the corrosion protection of DLC films. Diam Relat Mater 2002; 11: 160–8. doi:10.1016/S0925-9635(01)00568-4.

[67] Li Q, Thangadurai V. Synthesis, structure and electrical properties of Mo-doped CeO_2-Materials for SOFCs. Fuel Cells 2009; 9: 684–98. doi:10.1002/fuce.200900044.

[68] Chinarro E, Jurado JR, Figueiredo FM, Frade JR. Bulk and grain boundary conductivity of $Ca_{0.97}Ti_{1-x}F_xO_{3-\delta}$ materials. Solid State Ionics 2003; 160: 161–8. doi:10.1016/S0167-2738(03)00151-6.

[69] Li Q, Xia T, Liu XD, Ma XF, Meng J, Cao XQ. Fast densification and electrical conductivity of yttria-stabilized zirconia nanoceramics. Mater Sci Eng B Solid-State Mater Adv Technol 2007; 138: 78–83. doi:10.1016/j.mseb.2006.12.012.

[70] Cavigliasso GE, Esplandiu MJ, Macagno VA. Influence of the forming electrolyte on the electrical properties of tantalum and niobium oxide films: An EIS comparative study. J Appl Electrochem 1998; 28: 1213–9. doi:10.1023/A:1003449917148.

[71] Kerrec O, Devilliers D, Groult H, Chemla M. Dielectric properties of anodic oxide films on tantalum. Electrochim Acta 1995; 40: 719–24. doi:10.1016/0013-4686(94)00330-4.

[72] Michaelis A. Valve Metal, Si and Ceramic Oxides as Dielectric Films for Passive and Active Electronic Devices. vol. 10. 2008. doi:10.1002/9783527625307.ch1.

[73] Shimizu K, Brown G., Habazaki H, Kobayashi K, Skeldon P, Thompson G., et al. Direct observation of anodic films formed on tantalum in concentrated phosphoric and sulphuric acid solutions. Corros Sci 1998; 40: 963–73. doi:10.1016/S0010-938X(98)00035-3.

[74] Chaneliere C, Autran JL, Devine RAB, Balland B. Tantalum pentoxide (Ta_2O_5) thin films for advanced dielectric applications. Mater Sci Eng R Reports 1998; 22: 269–322. doi:10.1016/S0927-796X(97)00023-5.

[75] Diaz B, Swiatowska J, Maurice V, Seyeux A, Härkönen E, Ritala M, Tervakangas S,

Kolehmainen J, Marcus P. Tantalum oxide nanocoatings prepared by atomic layer and filtered cathodic arc deposition for corrosion protection of steel: Comparative surface and electrochemical analysis. Electrochim Acta 2013; 90: 232-245. doi:10.1016/j.electacta.2012.12.007

[76] T.-K. Tsai, C.-G. Chao. The growth morphology and crystallinity of electroless NiP deposition on silicon. App Surface Sc 2004; 233: 180-190. doi:10.1016/j.apsusc.2004.03.014

[77] Turan C, Cora ÖN, Koç M. Contact resistance characteristics of coated metallic bipolar plates for PEM fuel cells - Investigations on the effect of manufacturing. Int J Hydrogen Energy 2012; 37: 18187–204. doi:10.1016/j.ijhydene.2012.09.042.

[78] Bai CY, Wen TM, Hou KH, Pu NW, Ger M Der. The characteristics and performance of AISI 1045 steel bipolar plates with chromized coatings for proton exchange membrane fuel cells. Int J Hydrogen Energy 2011; 36: 3975–83. doi:10.1016/j.ijhydene.2010.12.110.